Supplementary Information for

Built-in electric fields in heterostructured lamellar membrane with highly efficient charged mass rejection

Chongchong Chen[1,※], Xiaoli Wu[2,※], Jingjing Chen[1], Siyu Liu[1], Yongzheng Wang[1], Wenjia Wu[1], Jie Zhang[1], Jingtao Wang[1,2,*], Zhongyi Jiang[3,*]

[1]School of Chemical Engineering, Zhengzhou University, Zhengzhou 450001, P. R. China.

[2]Henan Institute of Advanced Technology, Zhengzhou University, Zhengzhou 450003, P. R. China.

[3]Key Laboratory for Green Chemical Technology of Ministry of Education, School of Chemical Engineering and Technology, Tianjin University, Tianjin 300072, P. R. China.

[※]These authors contributed equally to this work.

*Corresponding author.

E-mail addresses: jingtaowang@zzu.edu.cn (J. Wang); zhyjiang@tju.edu.cn (Z. Jiang)

Supplementary Information

Supplementary methods

Materials and chemicals

Nylon support membranes with about 200 nm pore size and 50 mm diameter were supplied from Tianjin Jinteng Experimental Equipment Co., Ltd. Cyanic acid (98.0%), boric acid (99.5%), melamine (99.0%), sodium nitrate (99.0%), sodium sulfate anhydrous (99.0%), albumin from bovine serum (96.0%), pyridine (99.0%), propionic acid (99.0%), ethylenediamine (99.0%), acetic acid, sodium hypochlorite pentahydrate, sucrose, methylene blue (MB), methyl orange (MO), and rhodamine B (RhB) were purchased from Shanghai Aladdin Biochemical Technology Co., Ltd. Theophylline (≥99.0%), potassium chloride (99.5%), sodium chloride (99.5%), lithium chloride anhydrous (99.0%), calcium chloride anhydrous (99.9%), magnesium chloride (99.0%), and boron nitride powder (99.9%, 5~10 μm) were obtained from Shanghai Macklin Biochemical Co., Ltd. Isopropanol, ethanol and acetone were obtained from Tianjin Kemiou Chemistry Reagent Co., Ltd. Ammonia and nitrogen were supplied from Zhengzhou Zezhong Technology Co., Led. Note that the materials were used as received without further purification, and the deionized water was used throughout the experiment.

Characterizations

The structure and thickness of nanosheets and membranes were observed by atomic force microscopy (AFM, Bruker Dimension Fast Scan) and scanning electron microscopy (SEM, Auriga FIB SEM, Zeiss, Germany). The specific morphology of nanosheets and channel size were further characterized by high-resolution transmission electron microscopy (HRTEM, Tecnai G2F20, FEI, USA). Besides, the chemical microenvironment of membranes was tested by fourier transform infrared with wavelength from 400 to 4000 cm^{-1} (FTIR, Nicolet MAGNA-IR560 instrument), X-ray photoelectron spectroscopy (XPS, Escalab 250Xi, Thermo Fisher Scientific, U.S) and Zeta-potential measurements (Malvern Panalytical, NS-90Z). X-ray diffraction (XRD) was measured on Bruker D8 Advance ECO with the solvated state

of membranes and dry powder samples. The hydrophilicity/hydrophobicity of membranes with different time was evaluated through contact angle measuring instrument (model OCA 25, Germany).

Desalination performance test of BN/C_3N_4 membranes

Water permeance and salt rejection were evaluated firstly by forward osmosis experiments with 60 mL of 0.1 M salt solution and 2 M sucrose solution in the feed and draw compartments, respectively. The difference of osmotic pressure between the feed side (NaCl, 0.1 mol L^{-1}) and draw side (sucrose, 2 mol L^{-1}) provided a driving force to selective transport of water and salts. And the effective osmotic pressure of 44.5 bar was obtained by van't Hoff equation:

$$\pi = iCRT \tag{1}$$

where i is the numbers of ions or molecules dispersed into the corresponding solution (i_{NaCl} = 2, $i_{sucrose}$ =1), C is the molar concentration, R is the gas constant of 8.31 kPa L K^{-1} mol^{-1}, and T is the Kelvin temperature. The water permeance (J_w, L m^{-2} h^{-1} bar^{-1}) was obtained according to equation of (4):

$$J_w = \frac{\Delta V}{A \times \Delta P \times t} \tag{2}$$

where ΔV, A, and ΔP represent the liquid volume change between permeate side and draw side (L), effective membrane area (m^{-2}), and effective osmotic pressure (bar), respectively. Here, the testing time was chosen as 5 h to evaluate salt rejection and the corresponding water permeance.

Salt rejection could be calculated by monitoring ion concentration in permeate side through the following equation:

$$J_r = \frac{C_d}{C_f} \tag{3}$$

where J_r, C_d, and C_f denote the salt rejection, the concentration of permeate side, and feed side, respectively.

In this work, for better replicating the practical desalination process, multistage nanofiltration was performed to separate real seawater by home-made dead-end

device at 2 bar. The performance calculation is consistent with the equations of forward osmosis.

Chlorine exposure evaluation

Chlorine resistance was estimated by soaking membrane in an aqueous solution of sodium hypochlorite with ultrahigh active chlorine 10000 ppm at room temperature. The soaked membrane was immediately washed using water before testing. Here, to quantify chlorine exposure intensity, the product of active chlorine concentration and exposure time were used as a function of time. Chlorine resistance was demonstrated by normalized salt rejection and water permeance through the following equation:

$$R_i = \frac{R}{R_0} \tag{4}$$

where R_0 and R represent the initial rejection and instantaneous rejection at different times, respectively.

$$F_i = \frac{F}{F_0} \tag{5}$$

where F_0 and F denote initial water permeance and instantaneous water permeance at different times, respectively.

Supplementary notes

Note S1 The calculation of theoretical horizontal transfer distance during a collision

It is well known that charged ion transfers in a flat parabola within the parallel plates with uniform electric fields, as shown blow:

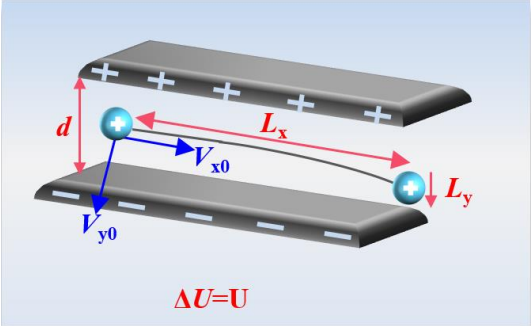

Here, the transport behavior of ions can be decomposed into uniform linear motion (V_x=V_{x0}, m s^{-1}) and uniform accelerated motion (V_y=V_{y0}+at, m s^{-1}) along the horizontal (L_x, m) and vertical (L_y, m) directions, respectively. The ion transport distance along L_x is determined by the time (t, s) that ion reaches channel walls along the vertical direction. Note that V_y is zero when the ion is perpendicular to the electric field direction. And V_x is equal to V_0. Thus, the collision time can be obtained by Newton's second law (6), electric field force equation (7), and uniformly accelerated motion formula:

$$F = ma \tag{6}$$

where F, m, a represent the external force applied (N), mass (kg), and acceleration (m s^{-2}), respectively.

$$F = ma = qE = q\frac{U}{d} \tag{7}$$

where q, E, U, d represent the ion charge (C), electric field intensity (V m^{-1}) within nanochannels, potential difference (V) between upper and lower two nanodomains, and vertical distance along the channel (m), respectively.

$$L_y = \frac{qU}{2md}t^2 \tag{8}$$

where t is time that ion reaches channel walls along the vertical direction. In this experiment, taking Na^+ as example, q is 1.602×10^{-19} C, U is 77.8×10^{-3} V, m is 3.819×10^{-26} kg, d is 0.89 nm, and the maximum value of L_y is also 0.89 nm. Thus, the time can be obtained.

$$\mathrm{t} = \sqrt{\frac{2mdL_y}{qU}} = \sqrt{\frac{2\times3.818\times10^{-26}\times0.89\times10^{-9}\times0.89\times10^{-9}}{1.602\times10^{-19}\times77.8\times10^{-3}}} = 2.203 \ \ \mathrm{ps}$$

The initial velocity of the ion can be calculated by the time of ion transfer through the channel.

$$V_0 = \frac{5}{4.31} = 1.21 \ \ \mathrm{ms^{-1}}$$

where channel distance is 5 nm, and the transport time is 4.31 ns.

Thus, the horizontal transport distance can be obtained.

$$L_x = V_0\sqrt{\frac{2mdL_y}{qU}} = V_0\sqrt{\frac{2L_ym}{q}}\frac{d^{0.5}}{U^{0.5}} = 1.21\times2.203 = 2.67\times10^{-3} \ \ \mathrm{nm}$$

However, the actual average transport distance is about 0.3 nm by theoretical simulation, which spans two orders of magnitude.

To precisely describe ion transport property in heterogeneous channels, the ion transport model of equation (L_x) is amended as blow:

$$L_x = KV_o\sqrt{\frac{2L_ym}{q}}\frac{d^{0.45}}{U^2} \tag{9}$$

where K is a proportionality constant ($V^{1.5}$) that includes ion diameter and nanosheet thickness. And the exponent of U is adjusted from 0.5 to 2. Here, nanosheet thickness is about 1.2 nm. Considering that the diameter of Na^+ is 7.16×10^{-1} nm at full hydration, the actual hydration diameter was chosen as 2/3 of theoretical value.

Thus, the modified horizontal transport distance can be obtained.

$$L_x = KV_o\sqrt{\frac{2L_y m}{q}}\frac{d^{0.5}}{U^2}$$

$$= \frac{1.2}{0.716 \times 2/3}\sqrt{\frac{2 \times 3.818 \times 10^{-26} \times 0.89 \times 10^{-9}}{1.602 \times 10^{-19}}}\frac{(0.89 \times 10^{-9})^{0.5}}{(77.8 \times 10^{-3})^2}$$

$$= 0.255 \text{ nm}$$

This is comparable to the actual average transport distance.

Likewise, for anion of Cl^-, q is 1.602×10^{-19} C, U is 77.8×10^{-3} V, m is 5.889×10^{-26} kg, d is 0.89 nm, the maximum value of L_y is also 0.89 nm, nanosheet thickness is 1.2 nm, and theoretical hydration diameter of Cl^- is 6.64×10^{-1} nm.

The initial velocity of Cl^- can be obtained.

$$V_0 = \frac{5}{3.54} = 1.41 \text{ ms}^{-1}$$

Then, the horizontal transport distance is obtained.

$$L_x = V_0\sqrt{\frac{2L_y m}{q}}\frac{d^{0.5}}{U^{0.5}} = 1.41\sqrt{\frac{2 \times 5.889 \times 10^{-26} \times 0.89 \times 10^{-9}}{1.602 \times 10^{-19}}}\frac{(0.89 \times 10^{-9})^{0.5}}{(77.8 \times 10^{-3})^{0.5}}$$

$$= 3.86 \times 10^{-3} \text{ nm}$$

The actual average transport distance is about 0.4 nm, which is two orders of magnitude higher that the theoretical value.

However, the modified horizontal transport distance is calculated to be:

$$L_x = KV_o\sqrt{\frac{2L_y m}{q}}\frac{d^{0.5}}{U^2}$$

$$= \frac{1.2}{0.664 \times 2/3}\sqrt{\frac{2 \times 5.889 \times 10^{-26} \times 0.89 \times 10^{-9}}{1.602 \times 10^{-19}}}\frac{(0.89 \times 10^{-9})^{0.5}}{(77.8 \times 10^{-3})^2}$$

$$= 0.342 \text{ nm}$$

And the value of horizontal transport distance is consistent with the actual average transport distance.

Note S2 Calculation of apparent diffusion coefficient

Fick's law is employed to quantify the diffusion coefficient of ions through the membrane under concentration gradient, as shown below:

$$J = -D\frac{d_c}{d_x} \tag{10}$$

where J, D, dc, and dx represent the diffusion flux (mol m^{-2} h^{-1}), diffusion coefficient (m^2 s^{-1}), concentration gradient (mol m^{-3}), and diffusion distance (m), respectively. The '-' means the diffusion direction is opposite to that of concentration gradient.

Taking Na^+ as example under potential difference of 71.5 mV, J is 2.43×10^{-6} mol m^{-2} h^{-1}, dc is 0.2×10^{3} mol m^{-3}, and dx is 1920×10^{-9} m.

Thus, the diffusion coefficient could be obtained by the following equation.

$$D = -\frac{Jd_x}{d_c} = -\frac{2.43\times10^{-6}\times1920\times10^{-9}}{0.2\times10^{3}} = -2.33\times10^{-14}\ \ (\mathrm{m^2\ \ s^{-1}})$$

Supplementary figures

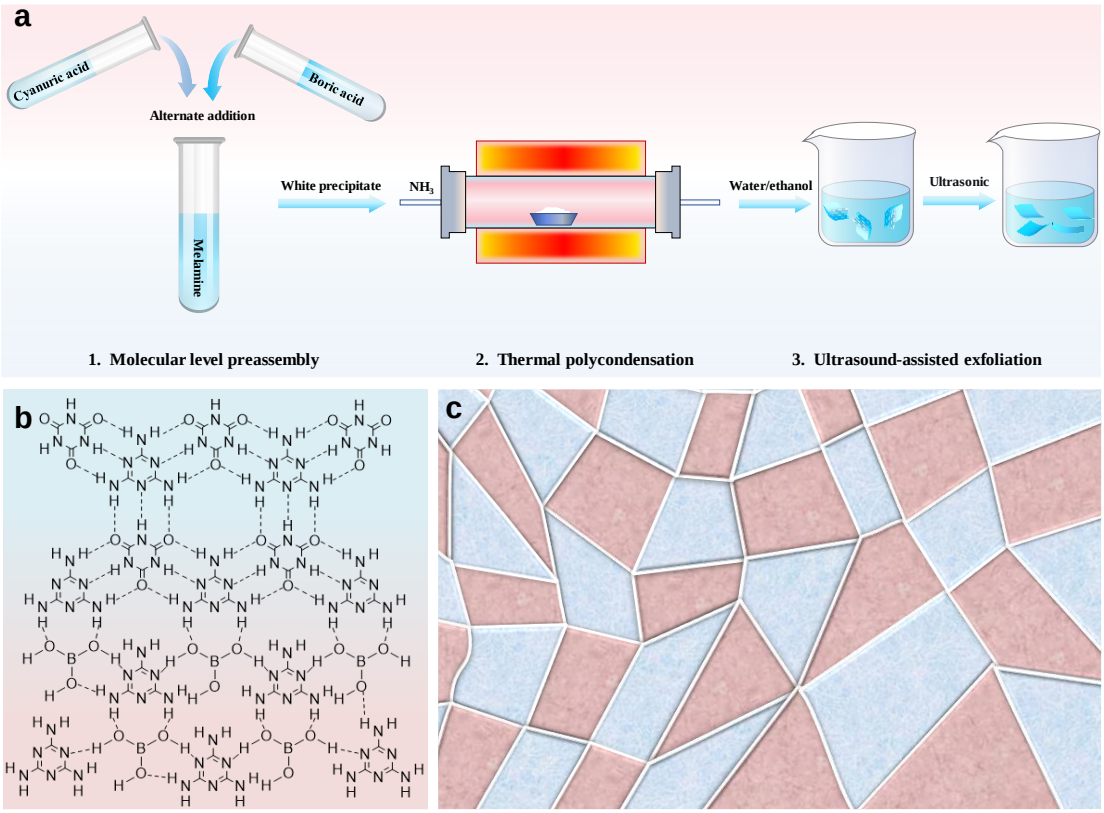

Supplementary Figure 1. (a) Schematic diagram of preparation process for heterostructured nanosheets. (b) The topological network structure of precursors for BN/C_3N_4. (c) The diagram of BN/C_3N_4 (Pike represents the negatively charged nanodomains, blue represents the positively charged nanodomains).

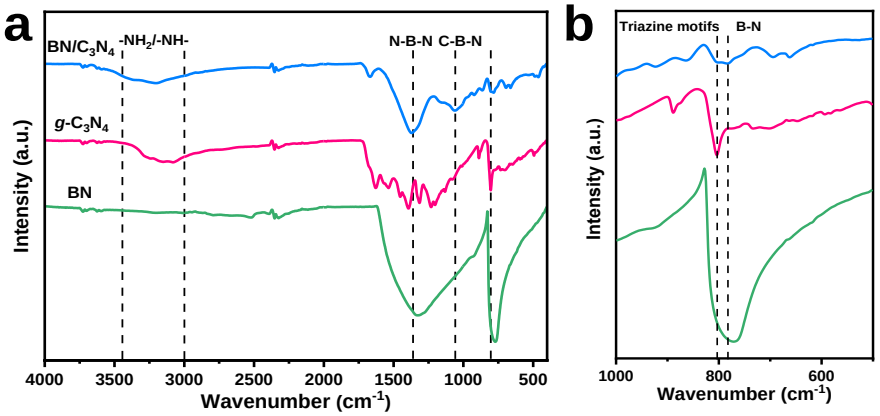

Supplementary Figure 2. (a) The FTIR spectra of membranes and (b) the corresponding amplification peak.

A broad peak near 3100 cm^{-1} is contributed to the $–NH_2$ or –NH– groups at the aromatic ring for BN/C_3N_4. The peaks at the range of 769 – 828 cm^{-1} correspond to the typical breathing mode of triazine motifs on the *g*-C_3N_4 and stretching vibration of B-N on the BN. Especially, the BN/C_3N_4 show the typical characteristic peaks of *g*-C_3N_4 (triazine motifs, $–NH_2$ or –NH–) and BN (N–B–N, B–N), indicating the existence of independent *g*-C_3N_4 and BN nanodomains in the heterostructured nanosheets.

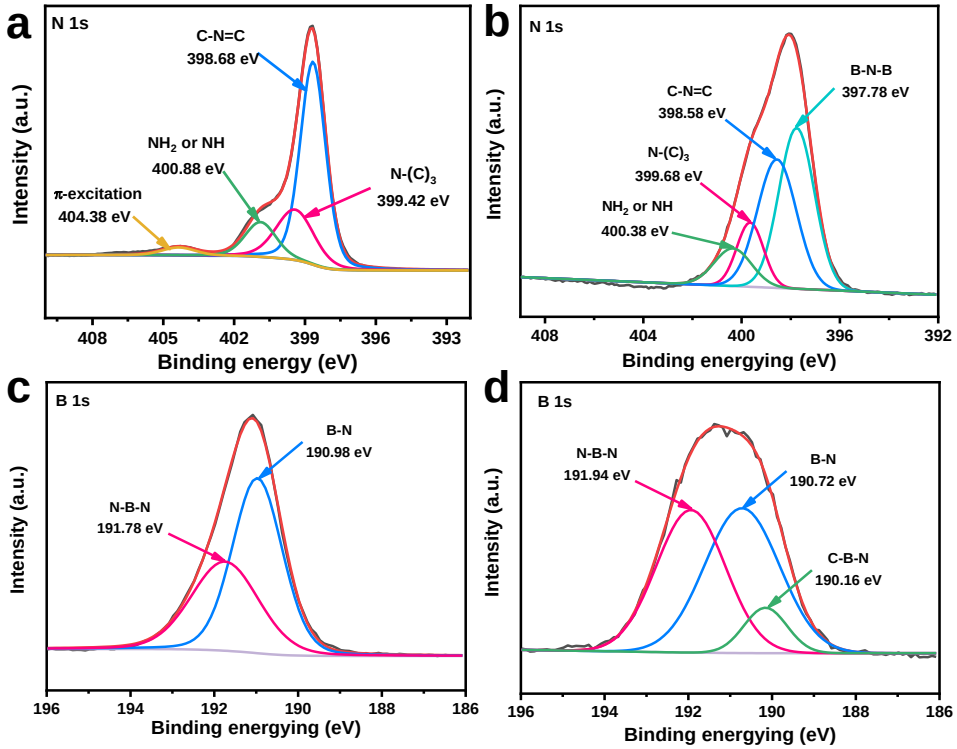

Supplementary Figure 3. N1s XPS spectra of (a) *g*-C_3N_4 and (b) BN/C_3N_4. B 1s XPS spectra of (c) BN and (d) BN/C_3N_4.

The high resolution N 1s spectrum of *g*-C_3N_4 could be divided into four peaks at 398.68, 399.42, 400.88 and 404.38 eV, which correspond to the sp^2-bonded N in triazine rings, bridging N atoms in N–$(C)_3$, the terminal amino groups (NH_2 or NH) and π-excitations, respectively. Likewise, the N 1s spectrum of BN/C_3N_4 also reveals four peaks. The dominant peak at 397.78 eV is ascribed to the B–N–B, while the peaks at 398.58, 399.68, and 400.38 eV correspond to the C–N=C, N–$(C)_3$, and –NH_2 or –NH– groups. Besides, compared with the BN, the emerging peak of C-B-N could be observed in B 1s spectrum of BN/C_3N_4.

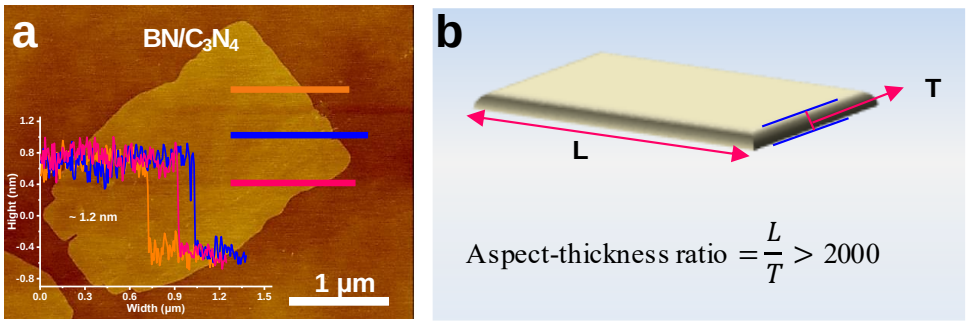

Supplementary Figure 4. (a) The AFM image of BN/C_3N_4 (inset: the corresponding height profile). (b) The diagram of a nanosheet.

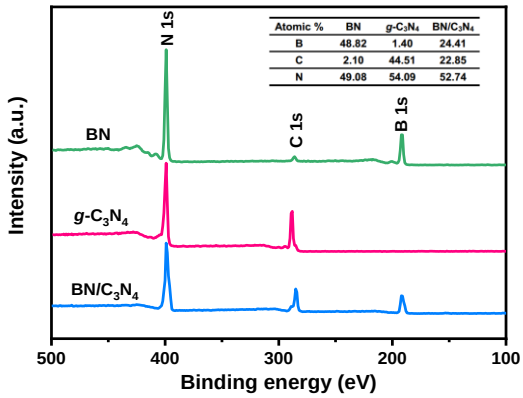

Supplementary Figure 5. XPS spectra of nanosheets.

The atom ratio of B to N is close to 1.0 in BN nanosheets. The atom ratio of C to N is 1.22 in *g*-C_3N_4 nanosheets, which is different from the theoretical ratio of 1.33. This should come from carbon adsorbed on the material surface. XPS reveals that the content of B, C, and N in BN/C_3N_4 is 24.41%, 22.85%, and 52.74%, respectively. Here, the content of B (BN) is 24.41% as one case, the ratio of C (*g*-C_3N_4) is

$$\frac{52.74\% - 24.41\%}{1.33} = 21.30\%$$

Considering the carbon adsorption at the material surface, it is reasonable to assume that the ratio of BN and *g*-C_3N_4 nanodomains is comparable.

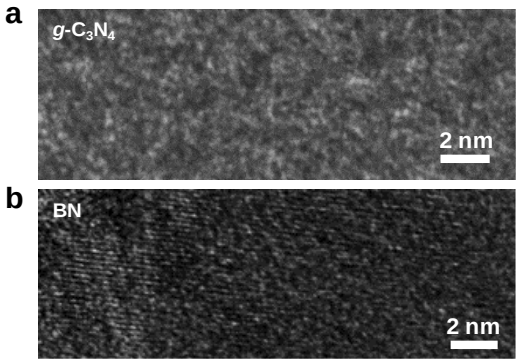

Supplementary Figure 6. HRTEM images of (a) *g*-C_3N_4 and (b) BN nanosheets.

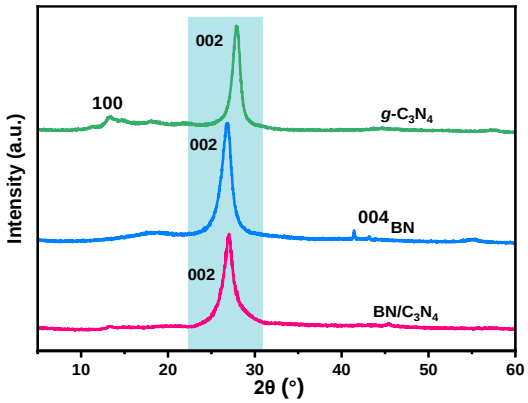

Supplementary Figure 7. XRD patterns of nanosheets.

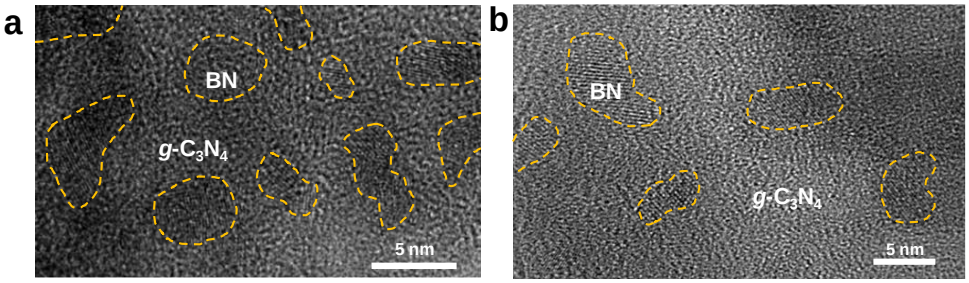

Supplementary Figure 8. HRTEM images of BN/C_3N_4 nanosheets with (a) the nanodomain size of 3 ~ 6 nm and (b) proportion of 1:3 (BN:*g*-C_3N_4).

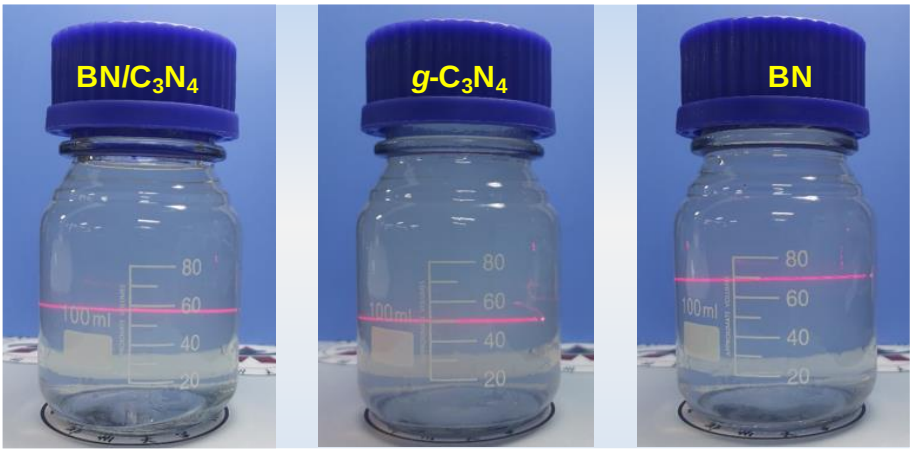

Supplementary Figure 9. The photos of nanosheet solution.

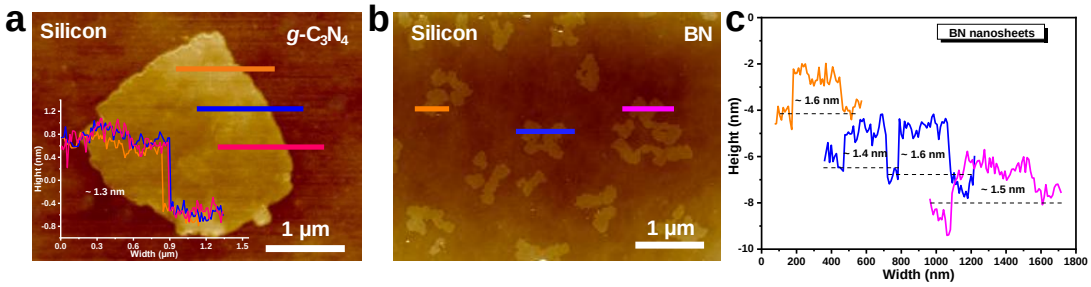

Supplementary Figure 10. (a) The AFM image of *g*-C_3N_4 nanosheet (inset: the corresponding height profile). (b) The AFM image of BN nanosheets and (c) the corresponding height profile.

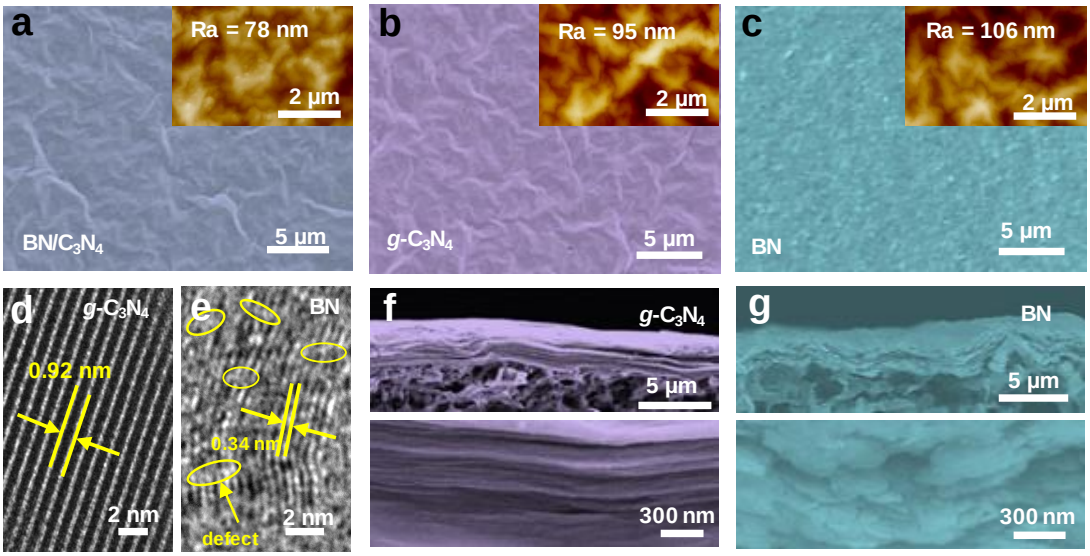

Supplementary Figure 11. The surface SEM images and corresponding surface AFM images of (a) BN/C_3N_4, (b) *g*-C_3N_4, and (c) BN membranes. HRTEM images of (d) *g*-C_3N_4 and (e) BN membranes. Cross-sectional SEM images and high-resolution SEM image of (f) *g*-C_3N_4 and (g) BN membranes.

Note that the stacking of BN nanosheets leaves an intersheet *d* spacing of about 2.0-2.5 nm (Supplementary Fig. 11e), which is consistent with the observation in the literature[1]. Considering the electronic clouds around BN nanosheets occupying 0.35 nm, and the BN nanosheets with thickness of ~1.5 nm possess about 4 layer. Thus, the effective size of channel is about 0.6-1.1 nm.

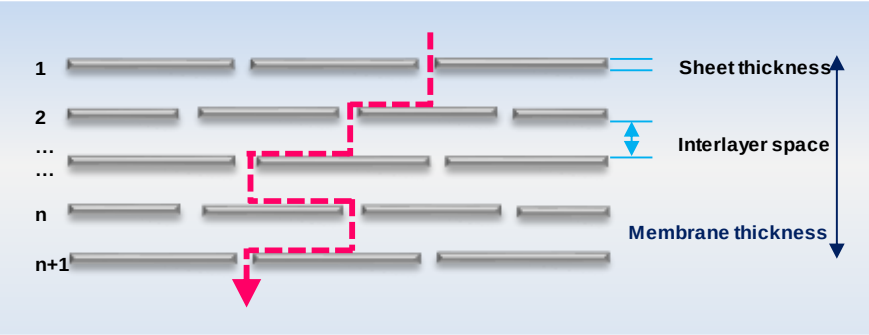

Supplementary Figure 12. Schematic diagram of molecule/ion transport paths through lamellar membrane.

The theoretical transport distance of ions through lamellar membrane can be evaluated by the following equation[2]:

$$L' = \frac{L}{2} \times \frac{I}{d + w}$$

where *L*', *L*, *I*, *d* and *w* denote the theoretical transport distance, nanosheet size, membrane thickness, interlayer distance and nanosheet thickness, respectively.

In this work, taking BN/C_3N_4 as example, *L* is 3000 nm, *I* is 1920 nm, *d* is 0.89 nm, and *w* is 1.2 nm.

$$\frac{L'}{I} = \frac{L}{2 \times (d + w)} = \frac{3000}{2 \times (0.89 + 1.2)} = 718$$

Thus, the transport path of ions through lamellar membrane is more than 700 times longer than the actual membrane thickness.

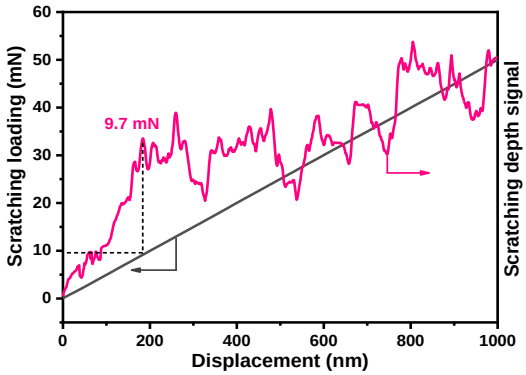

Supplementary Figure 13. Nanoscratch measurement of *g*-C_3N_4 membrane.

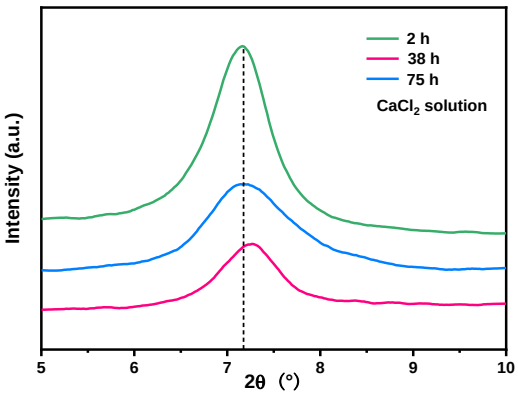

Supplementary Figure 14. XRD of BN/C_3N_4 membrane under $CaCl_2$ solution.

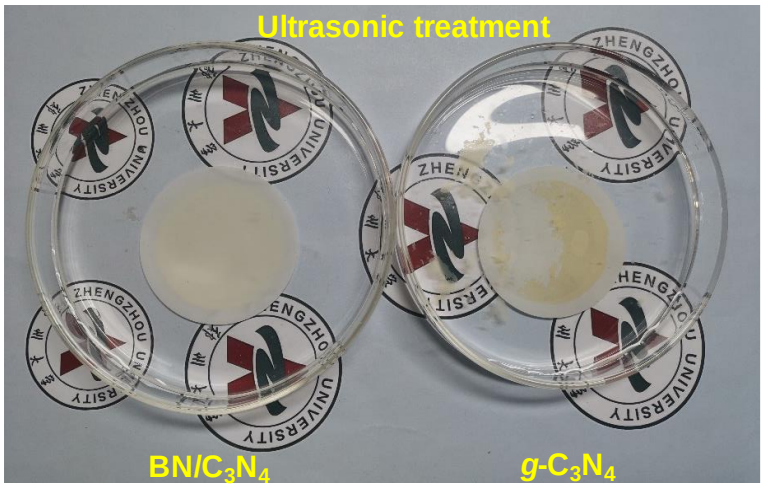

Supplementary Figure 15. The photos of membranes under ultrasound for 5 min at a power of 60 W.

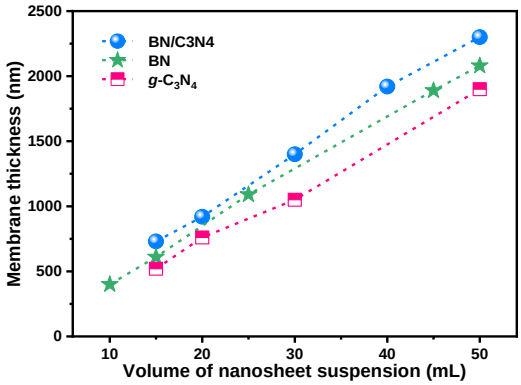

Supplementary Figure 16. Variation of membrane thickness with nanosheet loading.

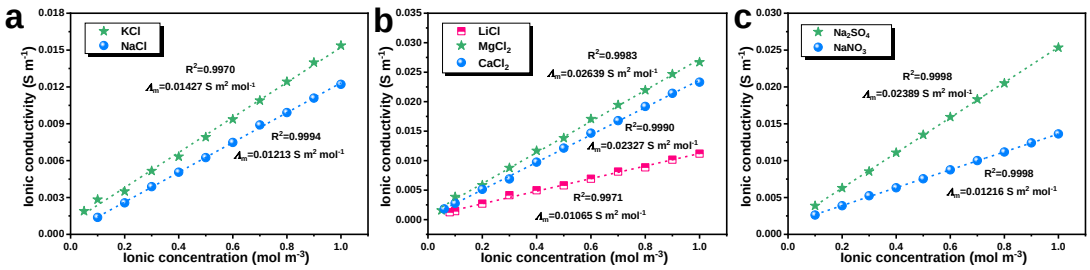

Supplementary Figure 17. Molar conductivity of different ions.

The ion concentration (C, mol m^{-3}) in the permeated side of different membranes was calculated by the following equation:

$$C = \frac{\lambda}{\Lambda_m}$$

where λ and Λ_m are the ion conductivity (S m^{-1}) in the permeated side and ion molar conductivity (S m^2 mol^{-1}), respectively.

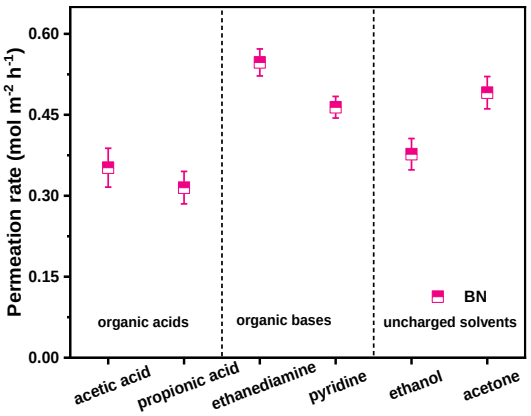

Supplementary Figure 18. Permeation rate of organic acids/bases through BN membranes.

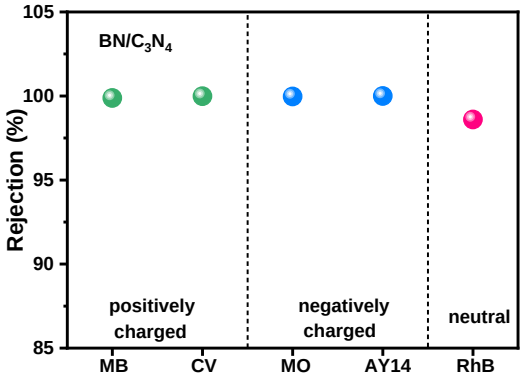

Supplementary Figure 19. The rejection of dyes with different electric charge through BN/C_3N_4 membrane under forward osmosis.

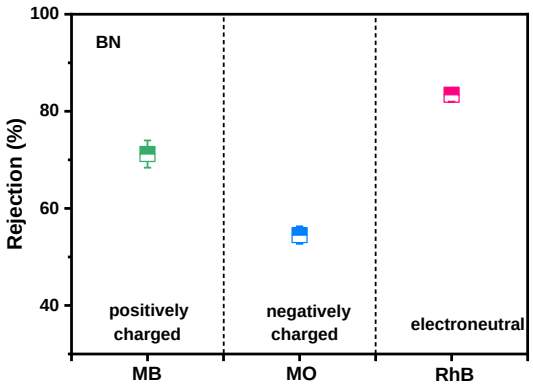

Supplementary Figure 20. The rejection of dyes with different electric charge through BN membrane.

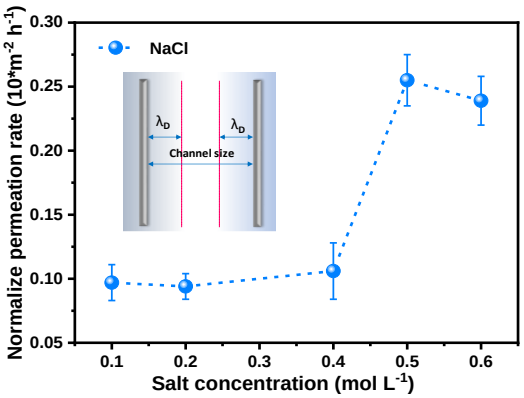

Supplementary Figure 21. NaCl permeation rate of *g*-C_3N_4 membrane with distinct feed concentration (inset: schematic illustration of Debye length and channel size).

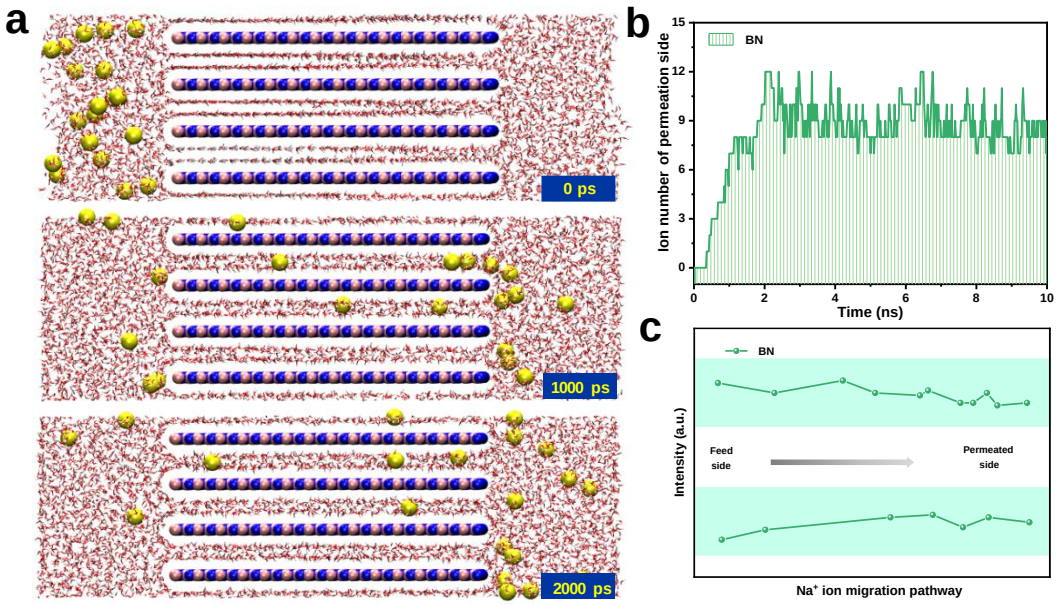

Supplementary Figure 22. (a) Simulation snapshots of Na^+ transporting through BN channels at 0, 1000 and 2000 ps. (b) The number of Na^+ in permeated side through BN channels. (c) Na^+ migration pathway through BN channels.

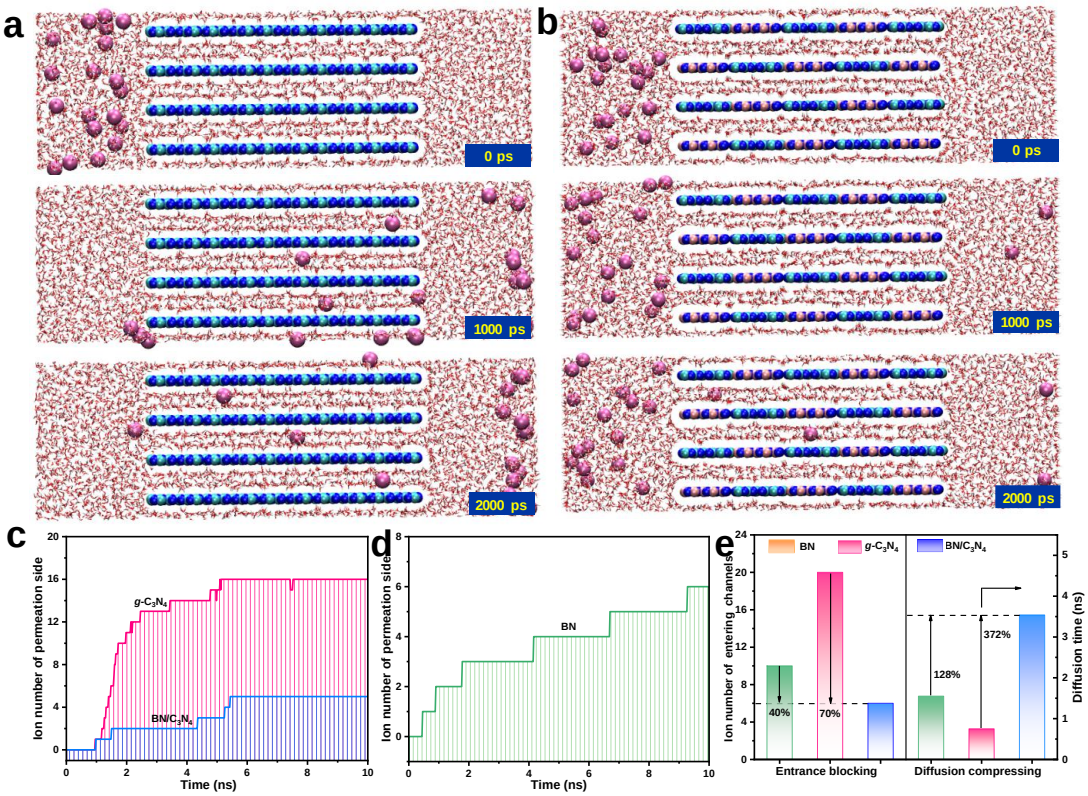

Supplementary Figure 23. Simulation snapshots of Na^+ transporting through (a) *g*-C_3N_4 channels and (b) BN/C_3N_4 channels at 0, 1000, and 2000 ps. Na^+ numbers in permeated side of (c) *g*-C_3N_4 and BN/C_3N_4 channels, and (d) BN channels. (e) Na^+ numbers of entering channels and corresponding diffusion time.

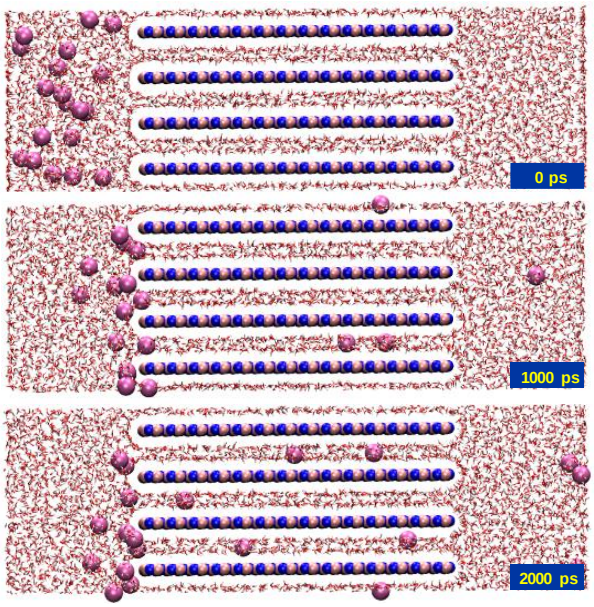

Supplementary Figure 24. Simulation snapshots of Na^+ transporting through BN channels.

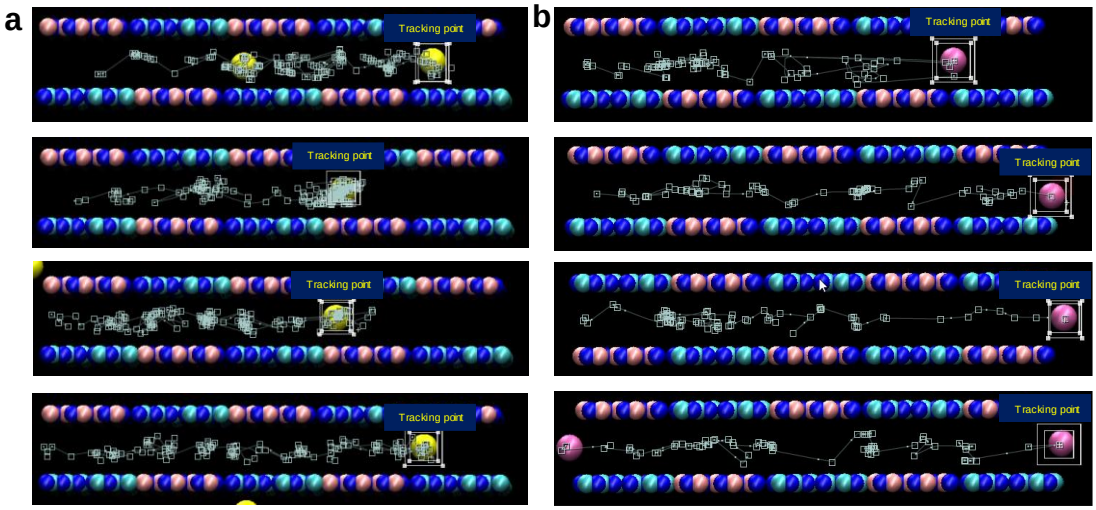

Supplementary Figure 25. The migration pathways of (a) Na^+ and (b) Cl^- in BN/C_3N_4 channels.

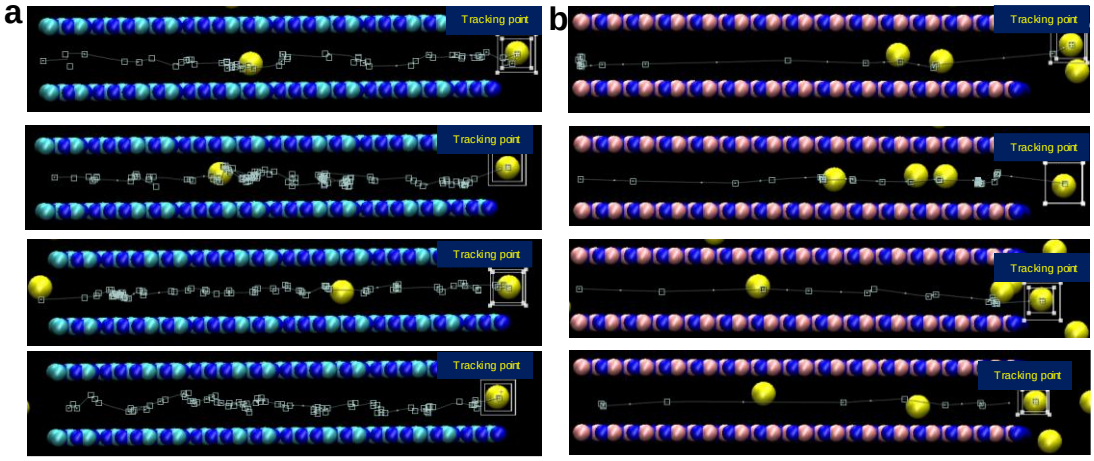

Supplementary Figure 26. Na^+ migration pathways through (a) *g*-C_3N_4 channels and (b) BN channels.

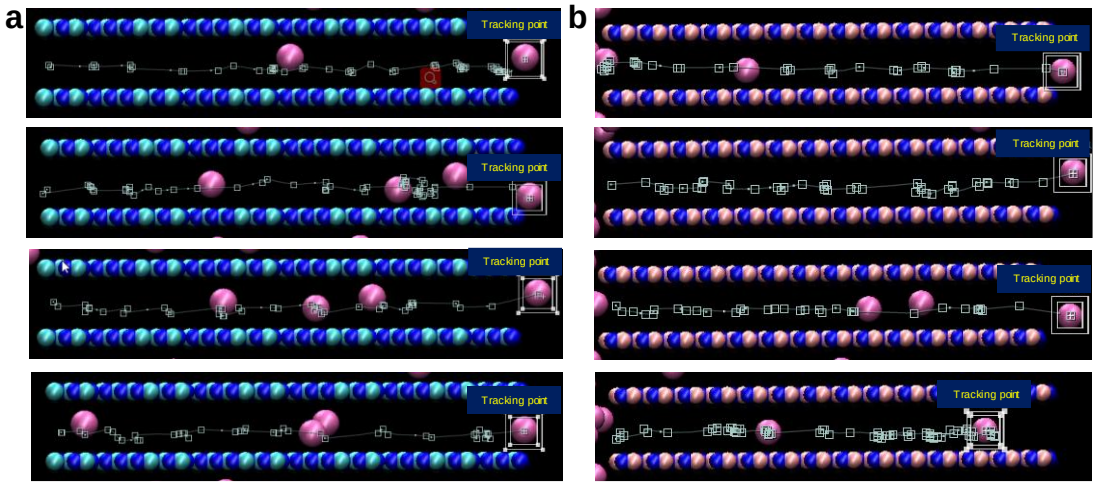

Supplementary Figure 27. Cl^- migration pathways through (a) *g*-C_3N_4 channels and (b) BN channels.

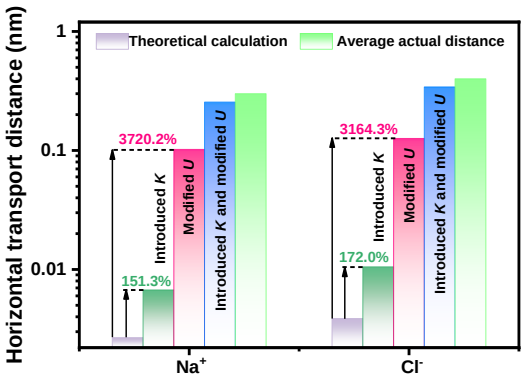

Supplementary Figure 28. The influence of introduced *K* and modified *U* on the horizontal transfer distance of ions.

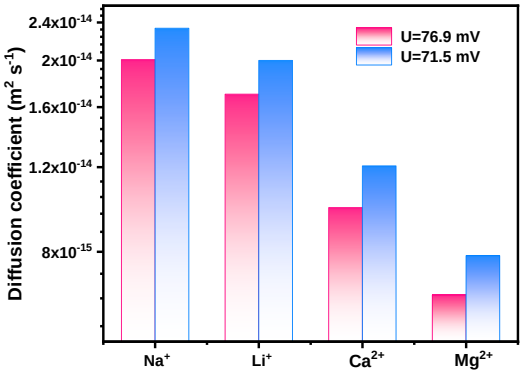

Supplementary Figure 29. The apparent diffusion coefficient of various ions through BN/C_3N_4 membranes under different potential difference.

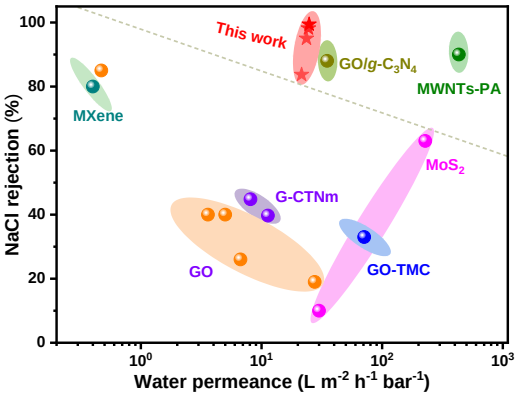

Supplementary Figure 30. The comparison of the NaCl rejection and water permeance between the BN/C_3N_4 and the membranes reported in literature under nanofiltration process.

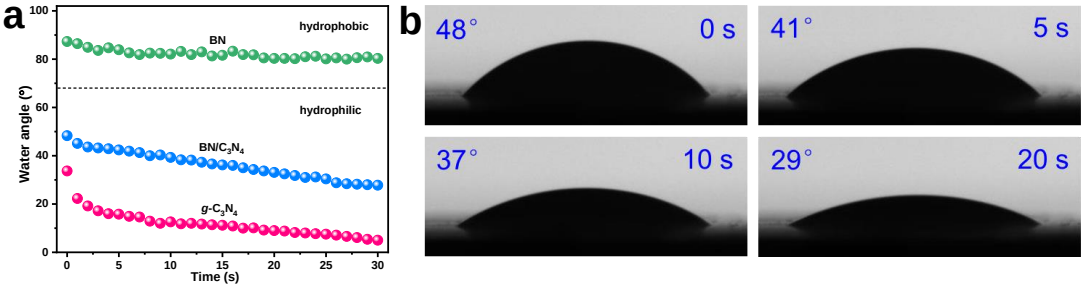

Supplementary Figure 31. (a) Dynamic water contact angle of membranes. (b) Water contact angle of BN/C_3N_4 membranes with different time.

Supplementary Tables

Table S1. The effective diameter and hydrated diameter of different cations and anions.

Ions	Effective ionic diameter (Å)	Hydrated diameter (Å)
K^+	2.66	6.62
Na^+	1.90	7.16
Li^+	1.20	7.64
Ca^{2+}	1.98	8.24
Mg^{2+}	1.30	8.56
Cl^-	4.42	6.64
NO_3^-	2.58	6.70
SO_4^{2-}	4.60	7.58

Table S2. Dye properties: molecular weights, charge, and chemical structures.

Dye molecules	Da	Charge	3D Molecule structure
Methyl orange (MO)	327.3	-	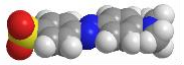
Methylene blue (MB)	373.9	+	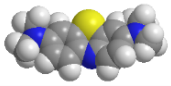
Crystal violet (CV)	408.5	+	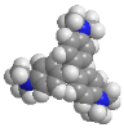
Acid yellow 14 (AY14)	449.2	-	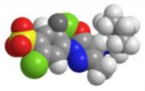
Rhodamine B (RhB)	479.0	electroneutral	—

Table S3. The performance comparison of different membranes under forward osmosis.

Membrane materials	Thickness (nm)	Operation mode	Feed salt concentration (M)	Permeance (mL m^{-2} h^{-1} bar^{-1})	Ion Rejection (%)	Ref.
FGOM-1	200	Forward osmosis	0.1	42.8	97.4	3
FGOM-30	200			30.2	99.5	3
	100			50.1	99.2	3
FGOM-60	200			22.6	99.7	3
PCGO	5000	Forward osmosis	0.1	7.0	97.0	4
	1000			33.0	94.0	4
KCl-GO	750	Forward osmosis	0.25	8.0	99.0	5
Non-covalent functionalized GOM	5300	Forward osmosis	0.2	34.6	95.0	6
Dye-functionalized MoS_2	5000	Forward osmosis	0.1	33.0	99.0	7
SCMM-80	526	Forward osmosis	0.1	59.5	97.0	8
SCMM-120	429			51.3	98.0	8
SCMM-180	401			51.5	98.0	8
Al^{3+}-intercalated MXMs	5580	Forward osmosis	0.1	96.0	92.3	9
	110			56.0	96.5	9
	270			22.0	99.6	9

Table S4. The salt composition of real seawater originating from the East China Sea.

Composition	KCl	NaCl	Na_2SO_4	$CaCl_2$	$MgCl_2$
M	0.0433	1.1490	0.1358	0.0261	0.2979

Table S5. The performance comparison of different membranes under nanofiltration process.

Membrane materials	Thickness (nm)	Feed salt concentration (M)	Water permeance (L m^{-2} h^{-1} bar^{-1})	Ion Rejection (%)	Ref.
(Cationic+anionic) porous MoS_2-s10	1000	500 mM	228.0	63	10
Earlier MoS_2	1000	20 mM	30	10	11
GO-TMC	18	20 mM	27.6	19	12
GO	~150	34 mM	~71	33	13
GO	~53	20 mM	~5	40	14
ATM-11.5	300	50 mg/L	0.4	80	15
GO/g-C_3N_4-3(II)	~2250	20 mM	~35	~88	16
GO60FLG	60	34 mM	~0.464	85	17
GO0FLG		34 mM	6.724	26	17
HYDRACoRe50		34 mM	3.63	40	18
MWNTs-polyamide membrane	100-300	10 mM	432	90	19
G-CNTm(4:1)		10 mM	8.05	44.8	20
G-CNTm(2:1)			11.33	39.7	20
BN/C_3N_4 membrane	~1900 nm	200 mM	21.5 23.6 24.5 24.8	83.7 95.1 98.2 99.4	This work

Supplementary references

1. Chen, C. *et al.* Ultrafast, stable ionic and molecular sieving through functionalized boron nitride membranes. *ACS Appl. Mater. Interfaces* **11**, 30430–30436 (2019).
2. Nie, L. *et al*. Realizing small-flake graphene oxide membranes for ultrafast size-dependent organic solvent nanofiltration. *Sci. Adv*. **6**, eaaz9184 (2020).
3. Qian, Y. *et al*. Enhanced ion sieving of graphene oxide membranes *via* surface amine functionalization. *J. Am. Chem. Soc*. **143**, 5080–5090 (2021).
4. Abraham, J. *et al*. Tunable sieving of ions using graphene oxide membranes. *Nat. Nanotechnol*. **12**, 546–550 (2017).
5. Chen, L. *et al*. Ion sieving in graphene oxide membranes *via* cationic control of interlayer spacing. *Nature* **550**, 380–383 (2017).
6. Ran, J. *et al*. Non-covalent cross-linking to boost the stability and permeability of graphene-oxide-based membranes. *J. Mater. Chem. A* **7**, 8085–8091 (2019).
7. Hirunpinyopas, W. *et al*. Desalination and nanofiltration through functionalized laminar MoS_2 membranes. *ACS Nano* **11**, 11082–11090 (2017).
8. Lu, Z. *et al*. Self-crosslinked MXene ($Ti_3C_2T_x$) membranes with good antiswelling property for monovalent metal ion exclusion. *ACS Nano* **13**, 10535–10544 (2019).
9. Ding, L. *et al*. Effective ion sieving with $Ti_3C_2T_x$ MXene membranes for production of drinking water from seawater. *Nat. Sustain*. **3**, 296–302 (2020).
10. Sapkota, B. *et al*. High permeability sub-nanometre sieve composite MoS_2 membranes. *Nat. Commun*. **11**, 2747 (2020).
11. Wang, Z. *et al*. Understanding the aqueous stability and filtration capability of MoS_2 membranes. *Nano letters* **17**, 7289–7298 (2017).
12. Hu, M. & Mi, B. Enabling graphene oxide nanosheets as water separation membranes. *Environ. Sci. Technol*. **47**, 3715–3723 (2013).
13. Akbari, A. *et al*. Large-area graphene-based nanofiltration membranes by shear alignment of discotic nematic liquid crystals of graphene oxide. *Nat. Commun*. **7**,

(2016).

14. Han, Y., Xu, Z. & Gao, C. Ultrathin graphene nanofiltration membrane for water purification. *Adv. Funct. Mater*. **23**, 3693–3700 (2013).
15. Zhu, J. *et al*. Precisely tunable ion sieving with an Al_{13}-$Ti_3C_2T_x$ lamellar membrane by controlling interlayer spacing. *ACS Nano* **14**, 15306–15316 (2020).
16. Wu, Y. *et al*. 2D heterostructured nanofluidic channels for enhanced desalination performance of graphene oxide membranes. *ACS Nano* **15**, 7586–7595 (2021).
17. Morelos-Gomez, A. *et al*. Effective NaCl and dye rejection of hybrid graphene oxide/graphene layered membranes. *Nat. Nanotechnol*. **12**, 1083–1088 (2017).
18. Yuan, Y. *et al*. Enhanced desalination performance of carboxyl functionalized graphene oxide nanofiltration membranes. *Desalination* **405**, 29–39 (2017).
19. Zhao, H. *et a*l. Improving the performance of polyamide reverse osmosis membrane by incorporation of modified multi-walled carbon nanotubes. *J. Memb. Sci*. **450**, 249–256 (2014).
20. Han, Y., Jiang, Y. & Gao, C. High-flux graphene oxide nanofiltration membrane intercalated by carbon nanotubes. *ACS Appl. Mater. Interfaces* **7**, 8147–8155 (2015).